Inverse Growth of Large Grain Size and Stable Inorganic Perovskite Micro-Nanowire Photodetectors

Guoqing Tong, Maowei Jiang, Dae-Yong Son, Longbin Qiu, Zonghao Liu, Luis K. Ono, and Yabing Qi*

Energy Materials and Surface Sciences Unit (EMSSU)
Okinawa Institute of Science and Technology Graduate University (OIST)
1919-1 Tancha, Onna-son, Kunigami-gun, Okinawa 904-0495, Japan
*Corresponding author: Yabing Qi, E-mail: Yabing.Qi@OIST.jp

ABSTRACT: Control of the forward and inverse reactions between perovskites and precursor materials is key to attaining high quality perovskite materials. Many techniques focus on synthesizing nanostructured $CsPbX_3$ materials (e.g., nanowires) via a forward reaction ($CsX + PbX_2 \rightarrow CsPbX_3$). However, lower solubility of inorganic perovskites and complex phase transition make it difficult to realize the precise control of composition and the length of nanowires using the conventional forward approach. Herein, we report a self-assembly inverse growth of $CsPbBr_3$ micro-nanowires (MWs) ($CsPb_2Br_5 \rightarrow CsPbBr_3 + PbBr_2 \uparrow$) by controlling phase transition from $CsPb_2Br_5$ to $CsPbBr_3$. Two-dimensional (2D) structure of $CsPb_2Br_5$ serves as nucleation sites to induce the initial $CsPbBr_3$ MW growth. Also, phase transition allows crystal rearrangement and slows down the crystal growth, which facilitates the MW growth of $CsPbBr_3$ crystals along the 2D planes of $CsPb_2Br_5$. A $CsPbBr_3$ MW photodetector constructed based on the inverse growth shows a high responsivity of 6.44 A W^{-1} and detectivity of ~10^{12} Jones. Larger grain size, high crystallinity and bigger thickness can effectively alleviate the decomposition/degradation of perovskites, which leads to storage stability over 60 days in moisture (45% relative humidity) and operational stability over 3000 min under illumination (400 nm, ~20.06 mW cm^{-2}).

KEYWORDS: *inorganic perovskite, micro-nanowire, inverse growth, photodetector, operational stability*

1. INTRODUCTION

Inorganic perovskite materials ($CsPbX_3$, X = I, Br or Cl) have shown a great potential for applications in solar cells, light-emitting diodes (LEDs), photodetectors (PDs) and lasers because of their remarkable physical and chemical characteristics (e.g., tunable bandgap, strong optical absorption, high carrier mobility and long diffusion length) and low-cost fabrication.[1-6] Besides inorganic perovskite based thin films and quantum dots, nanowires (NWs) / micro-nanowires (MWs) exhibit outstanding performance in optoelectronic devices. Because of the confined carrier transport in one-dimensional channels/structures, it has been reported that fast charge transport could be realized to improve the electric performance.[7] In addition, compared with perovskite thin films, these NWs tend to have large grain size and less grain boundaries, which would reduce the trap /defects density and recombination rate resulting in a long carrier lifetime of photogenerated carriers and low leak current.[7-11] For example, Eaton and coworkers synthesized inorganic single crystalline perovskite $CsPbBr_3$ NWs with well-defined facets, which is beneficial for the high quality laser cavities.[12] The Fabry-Pérot lasing was detected in $CsPbBr_3$ NWs with a low threshold (5 μJ cm^{-2}). In parallel, Yang and coworkers developed single-crystalline $CsPbI_3$ nanorods with a uniform diameter (~150 nm) and length (~2 μm).[13] These high quality single-crystalline nanorods show a reduced trap density and enhanced carrier mobility leading to high performance PD with a responsivity of 2920 A W^{-1} and a fast response time (τ_{rise}/τ_{fall}) (the photocurrent

increase from 10% to 90% (τ_{rise}) and decrease from 90% to 10% (τ_{fall}) of maximum) of 50/150 μs.

Several advanced techniques have been developed to synthesize perovskite NWs, including solution-phase synthesis and chemical vapor deposition (CVD).[14-17] The solution method is the simplest strategy, yet showing great advantage in the fabrication of NW arrays because a precise ratio of precursor materials can be controlled and it only requires low-temperature synthesis processes (< 80 °C).[18, 19] For instance, Zhang and coworkers used an anion-exchange method to realize the $CsPbX_3$ alloy NWs by controlling the reaction between $CsPbBr_3$ NWs and halide precursors.[20] However, the solution growth methods are usually affected by the solvent, surfactant and low-solubility of inorganic perovskite precursor materials, which has a significant influence on the formation/nucleation process and optical properties.[7, 21] In contrast, CVD as an alternative process provides advantage to be solvent-free and direct growth on the substrates.[22, 23] The vapor-based method employing vacuum systems allows researchers to achieve a stoichiometric and highly crystalline NWs due to the absence of any solvent or surfactant.[22, 24] In addition, impurities in precursor materials can be removed from the sublimed precursors at a high temperature during evaporation.[25] Furthermore, the composition, diameter, length and growth direction of NWs can be controlled by experimental conditions such as catalyst,[26] substrates,[17] growth pressure/temperature.[26, 27] Specifically, highly oriented NWs can be realized via a vapor-phase epitaxial growth on the crystalline substrates such as sapphire and mica substrates.[28] Chen and co-workers prepared high-quality $CsPbBr_3$ NWs along the [001] directions on mica (001)

substrates through a vapor-phase epitaxy technique.[28] In addition, the horizontally oriented $CsSnX_3$ (X = Br, I) NWs / MWs along [001] were realized on mica substrates via a vapor phase growth by Jin, Chen and coworkers.[29] Despite the great results achieved by vapor phase synthesis, the formation of NWs is favorable only at a high temperature (~600 ºC) or with the aid of catalyst in a high vacuum system, which represents an obstacle for their commercial application (especially on flexible substrates).[26, 30-32]

Most of inorganic perovskite NWs/MWs in recent reports are synthesized by a forward reaction mechanism.[26, 33] In this technique, CsX and PbX_2 are dissolved in a solvent (e.g., octadecene or DMF/DMSO)[10, 20] or evaporated in a vacuum system[17, 29] at the optimized temperature in order to attain the final products of $CsPbX_3$ NWs as follows (forward reaction): $CsX + PbX_2 \rightarrow CsPbX_3$. The low solubility of inorganic perovskite materials in solvents when considering solution-based processes or the high evaporation temperature (~600 ºC) as well as the capital cost of vacuum systems employed for vacuum-based processes (e.g., CVD), and the complex Cs-Pb-X phase diagram are not attractive for mass production of NWs using this forward route.[20, 22, 29, 34, 35] How to realize NWs/MWs with an ultralong length over 100 μm with simple and controllable processing is a challenge but a prerequisite for integrated semiconductor devices.[36] It is worth noting that many derivative phases exist in the Cs-Pb-Br phase diagram such as the two-dimensional (2D) structure of $CsPb_2Br_5$ and the zero-dimensional phase of Cs_4PbBr_6.[37-39] They easily convert to 3D $CsPbBr_3$ under certain conditions as follows (inverse reaction): $CsPb_2Br_5 \rightarrow CsPbBr_3 + PbBr_2$; $Cs_4PbBr_6 \rightarrow$

$CsPbBr_3$ + 3CsBr,[40, 41] and also can serve as nucleation sites to further promote the continuous growth of $CsPbBr_3$ following the Ostwald ripening mechanism.[42, 43]

In this work, we developed a catalyst/template-free and inverse growth of $CsPbBr_3$ MWs taking advantage of the synergy effect of a derivative phase transition and Ostwald ripening. The $CsPb_2Br_5$ precursor layer was first deposited on the substrates via vacuum vapor deposition and then annealed in air. $CsPb_2Br_5$ films were converted to $CsPbBr_3$ (accompanied by volatilization of $PbBr_2$) during post-annealing because of the inverse reaction between $CsPbBr_3$ and the $CsPb_2Br_5$ derivative phase ($CsPb_2Br_5 \rightarrow CsPbBr_3 + PbBr_2 \uparrow$) and thermodynamic stability of $CsPbBr_3$ (**Figure 1**a). During the annealing process, the 2D $CsPb_2Br_5$ serves as nucleation sites, and the intermediate phase of $CsPb_2Br_5$@$CsPbBr_3$ effectively slows down the crystal growth of $CsPbBr_3$ compared with forward growth. In parallel, the 2D layer structure of $CsPb_2Br_5$ can also serve as a template during the phase transition/decomposition from the 2D $CsPb_2Br_5$ to the 3D cubic $CsPbBr_3$ phase, which provides enough space and allows the crystal rearrangement (2D $\rightarrow$ 3D) in the structure. The above characteristics facilitate continuous growth of $CsPbBr_3$ crystals along the preferred orientation to form $CsPbBr_3$ MWs with an ultralong length of ~510 μm. Based on this inverse growth of $CsPbBr_3$ MWs, high performance photodetectors were realized with a high responsivity of 6.44 A W^{-1} and a response time of 301/242 ms. The devices also exhibited outstanding storage stability over 60 days in air (relative humidity RH ~ 45%) and operational stability under monochromatic light (400 nm, ~20.06 mW cm^{-2}) over 3000 min (Table 1) because of larger grain size, high crystallinity and bigger thickness. This inverse

growth of $CsPbBr_3$ MWs from the derivative phase offers a new way to fabricate perovskite NWs / MWs and shows potential for applications in future integrated devices.

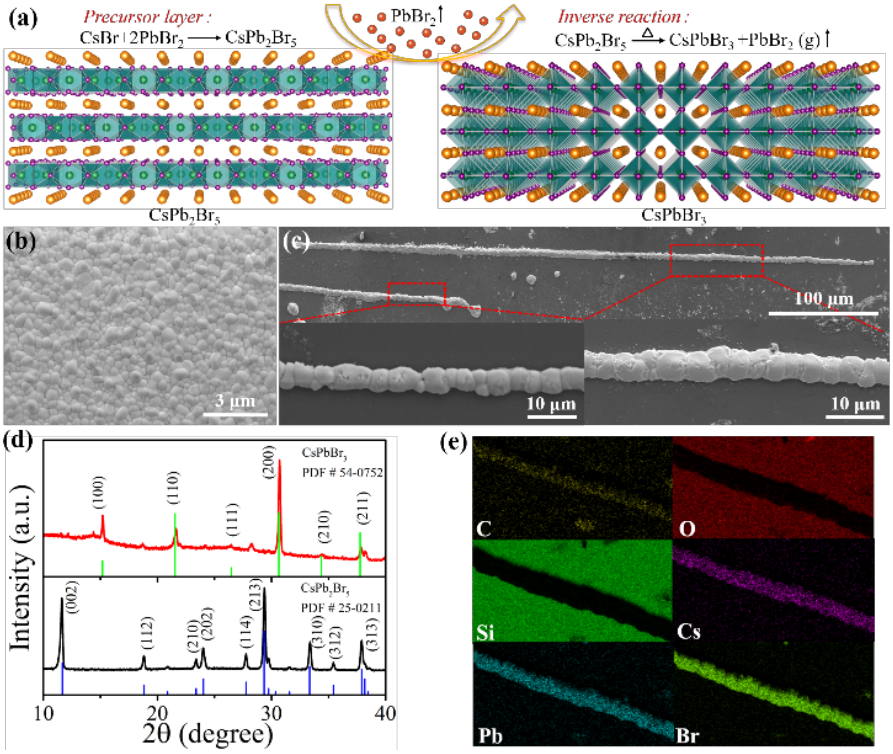

Figure 1. (a) The formation mechanism of $CsPbBr_3$ MW from $CsPb_2Br_5$ film after annealing at 450 °C for 1 h. SEM image of (b) the $CsPb_2Br_5$ film (250 °C) and (c) $CsPbBr_3$ MW. (d) XRD patterns of the $CsPb_2Br_5$ film (250 °C) and $CsPbBr_3$ NW. (e) EDS mapping of a $CsPbBr_3$ MW.

Table 1 Comparison of inorganic perovskite nanowires from previous works and this work.

Material	Formation direction	Method	Template	Length (μm)	Height (nm)	R (A W^{-1})	D* (Jones)	Operational Stability [min]	Storage Stability [h]	Ref
$CsPbBr_3$ MW	**Inverse**	**Vapor**	**No**	**~510**	**1360**	**6.44**	**2.88×10^{12}**	**3000**	**1440**	**This work**
$CsPbI_3$ NR	Forward	Solution	No	~2	—	2920	5.7×10^{13}	720	168	13
$CsPbI_3$ NW	Forward	Solution	No	＜20	—	—	—	140	—	44
$CsPbI_3$ NW	Forward	Solution	No	＞325	—	0.745	3.46×10^{10}	—	—	33
$CsPbBr_3$ NW	Forward	Vapor	Yes	~1500	—	4400	—	—	—	17

$CsPbBr_3$ NW	Forward	Vapor	No	~40	—	3306	7.9×10^{12}	—	—	26
$CsPbBr_3$ NW	Forward	Vapor	No	~20	~420	0.001	—	—	—	28
$CsPbBr_3$ NW	Forward	Solution	No	~12	—	—	—	—	—	45
$Cs_3Sb_2Cl_9$ NW	Forward	Solution	No	~0.29	4	3616	1.25×10^{6}	—	—	46
$CsPbI_3$ NW	Forward	Solution	Yes	＞150	250	1294	2.6×10^{14}	—	720 h	10
$CsPbI_3$ nanoarrays	Forward	Vapor	Yes	~10	~1000	0.0067	1.5×10^{12}	—	—	23
$CsPbBr_3$ nanoarrays	Forward	Vapor	No	＜30	20~1000	—	—	—	—	11
$CsPbBr_3$ nanoarrays	Forward	Solution	Yes	＞28	200	1377	—	—	—	19
$CsPbCl_3$ film	Forward	Vapor	—	—	—	0.1309	1.4×10^{13}	—	720 h	4
$CsPbBr_3$ film	Forward	Vapor	—	—	—	0.375	2.96×10^{11}	—	1560 h	39
$CsPbBr_3$ film	Forward	Solution	—	—	—	0.64	—	—	12	47
$Cs_3Cu_2I_5$ film	Forward	Solution	—	—	—	0.0649	6.9×10^{11}	—	—	48

※Operational stability is defined to be the stability when the device is under a bias and continuous light illumination.

2. RESULTS AND DISCUSSION

To grow $CsPbBr_3$ MWs, we first deposited the $CsPb_2Br_5$ thin film on the substrates, which served as a precursor layer. As seen in Figure 1a, $CsPb_2Br_5$ showed a 2D layer structure and was synthesized by excess $PbBr_2$ as follows:

$$CsBr + 2PbBr_2 \rightarrow CsPb_2Br_5$$

$$CsPbBr_3 + PbBr_2 \rightarrow CsPb_2Br_5$$

Therefore, we first deposited the $CsPb_2Br_5$ film with a thickness of 1 μm on the Si (100) /SiO_2 (300 nm) substrates by sequential vapor deposition as discussed in our previous

works.[41, 49] Then, we annealed the as-prepared films at 250 °C (20 min) in order to achieve high crystalline $CsPb_2Br_5$ grains. The scanning electron microscopy (SEM) image of the $CsPb_2Br_5$ film in Figure 1b showed a uniform and compact layer with high crystallinity after annealing. The atomic Cs/Pb/Br ratios determined by energy dispersive X-ray spectroscopy (EDS) mapping in Figure S1 was 1:2.3:5.2 in good agreement with the stoichiometry of the $CsPb_2Br_5$ phase. The structure of $CsPb_2Br_5$ was determined by X-ray diffraction (XRD). As seen in Figure 1d, characteristic peaks at 11.67°, 18.83°, 23.39°, 24.03°, 27.77°, 29.36°, 33.34°, 35.44° and 37.90° were assigned to (002), (112), (210), (202), (114), (213), (310), (312) and (313) diffraction planes of the tetragonal $CsPb_2Br_5$ phase at 250 °C, respectively, (Figure S2). After annealing $CsPb_2Br_5$ films at 450 °C for 1 h, ultralong $CsPbBr_3$ MWs (~510 μm) were obtained on the Si (100)/SiO_2 substrates (Figure 1c, S3). As shown in Figure 1d, the $CsPbBr_3$ MW showed a cubic phase (Figure S2). The peaks at 15.19°, 21.55°, 26.48°, 30.64°, 34.37°, and 37.77° can be assigned to (100), (110), (111), (200), (210) and (211) lattice planes, respectively. From the SEM images in Figure 1c, we found that the MWs were composed of grains connected to one another. The average grain size was over 5 μm. Additionally, the $CsPbBr_3$ MW also exhibited a height of 1.36 μm measured by atomic force microscopy (AFM) as shown in Figure S4, which was about 36% thicker than the precursor thickness of $CsPb_2Br_5$ layer, because of the growth of crystals and structure reconstruction during annealing following the Ostwald ripening mechanism.[42, 43] The length to height ratio of MW was 375. To further evaluate the chemical composition of MWs, we conducted EDS mapping on a single $CsPbBr_3$ MW (Figure 1e, S5). The single

MW was mainly composed of Cs, Pb and Br elements showing a uniform distribution. In addition, the Si and O elements were also detected suggesting the presence of a SiO_2 film around the MW. The EDS line scan was conducted to analyze the composition of the MW in Figure S6. A uniform elemental distribution of Cs, Pb and Br along the axial direction could be inferred with the estimated atomic Cs/Pb/Br ratios of 1:0.91:2.84, which was consistent with the stoichiometric ratio of the $CsPbBr_3$ phase.

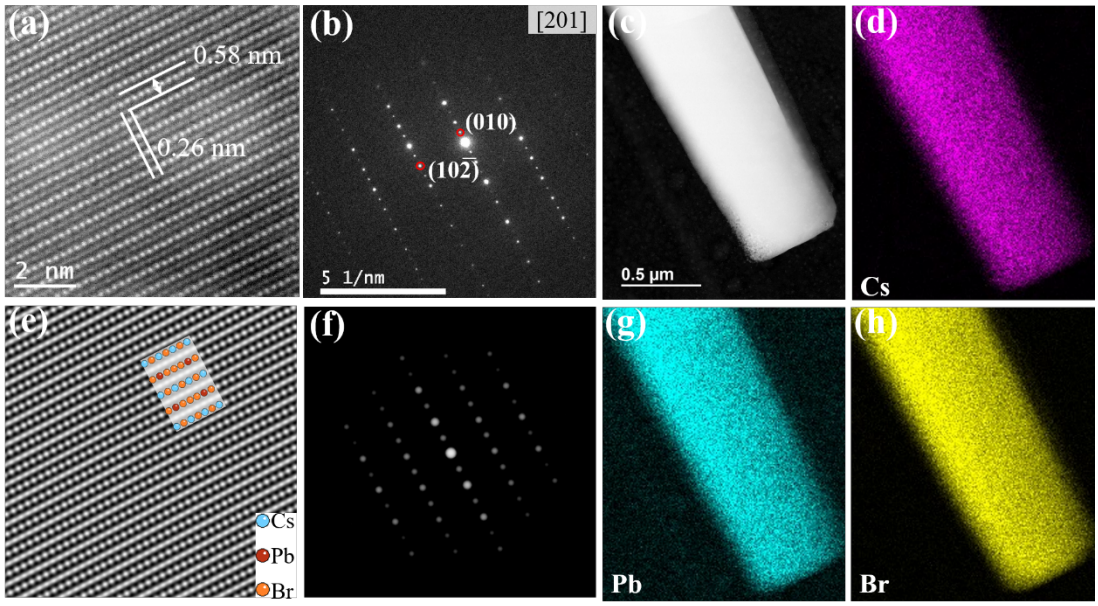

Figure 2. (a) STEM image resolving the lattice fringes and (b) SAED pattern of a $CsPbBr_3$ MW. (c) STEM image and corresponding EDS mapping of (d) Cs, (g) Pb and (h) Br. (e) Simulated lattice image and (f) SAED pattern of a $CsPbBr_3$ MW.

Based on Figure 1c, S4, our MWs exhibited a polycrystalline structure with oriented grains due to the self-assembly growth from the $CsPb_2Br_5$ film to $CsPbBr_3$ MWs during decomposition (inverse growth). However, each of the perovskite grains showed a single crystalline structure with a large grain size. To evaluate the crystallinity of the inversely grown $CsPbBr_3$ MWs, we conducted scanning transmission electron

microscopy (STEM) and selected-area electron diffraction (SAED) measurements (Figure 2a, b). The lattice fringes with a spacing of 5.8 Å and 2.6 Å in Figure 2a, respectively, correspond to the lattice spacing of (010) and $(10\bar{2})$ planes, along [201] zone axis of $CsPbBr_3$ (PDF#54-0752), which suggested the single crystalline nature of the grains in the $CsPbBr_3$ MWs. In addition, a simulation was calculated to find out the atom stacking along the [201] direction (Figure 2e). It was shown that the simulation agreed well with the collected STEM image (Figure 2a). The simulated SAED pattern (Figure 2f) also agreed well with the image in Figure 2b. Furthermore, a model of atom stacking image was added in Figure 2e, indicating that the rows with the dark contrast in Figure 2a might be derived from the secondary diffraction of the (010) plane. Importantly, the EDS mapping in Figure 2c, d, g and h showed a uniform element distribution of Cs, Pb and Br with the element ratios of 1:1:3 (Figure S7).

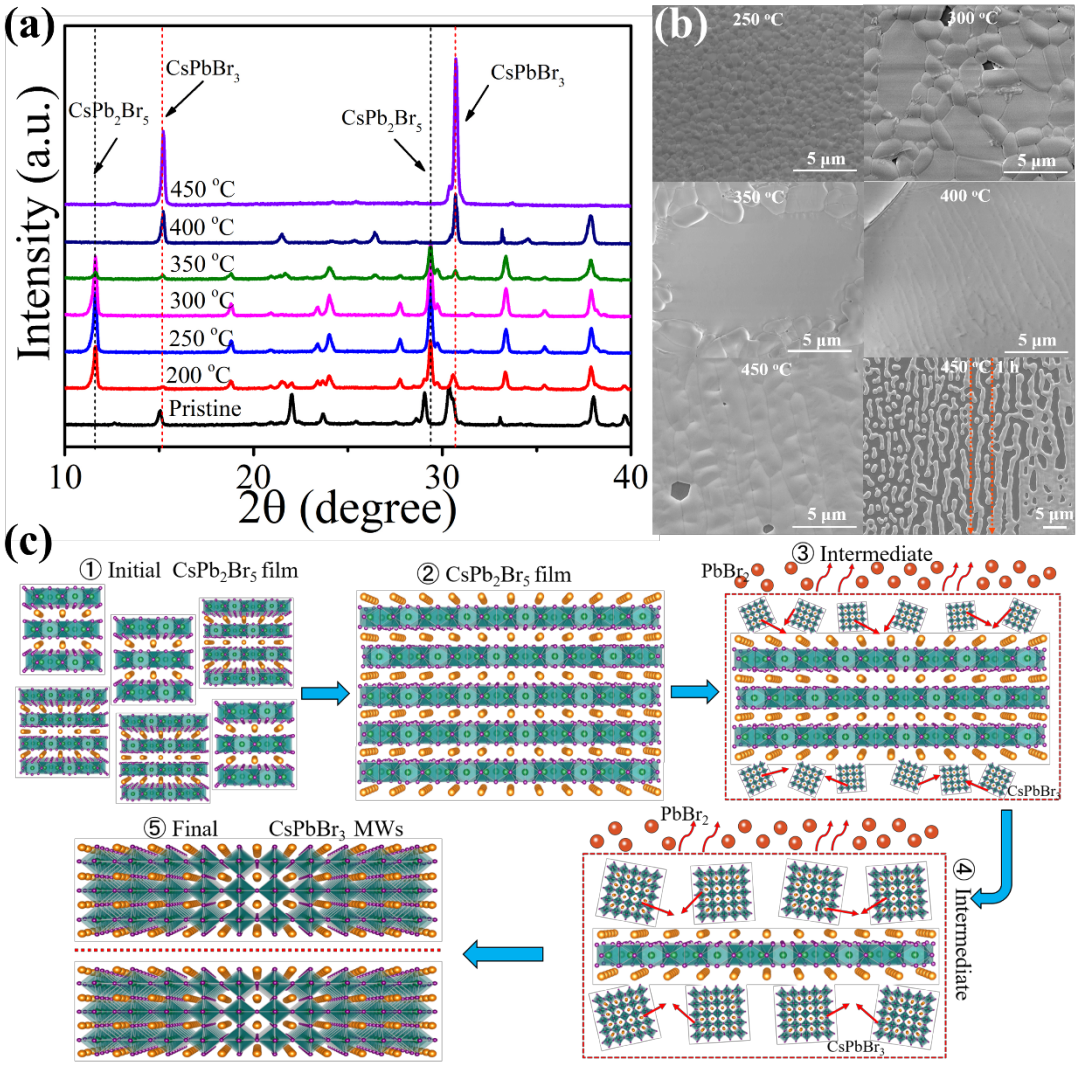

Figure 3. (a) XRD patterns of samples at different annealing temperatures. (b) SEM images of the as-prepared $CsPb_2Br_5$ film grown at 250 °C, 300 °C, 350 °C, 400 °C, 450 °C, for 20 min at each temperature, and 450 °C, for 1 h, respectively. (c) Schematic illustration showing the inverse growth of the samples from the $CsPb_2Br_5$ film to $CsPbBr_3$ MWs.

To further understand the inverse growth of $CsPbBr_3$ MWs, we first investigated the forward and inverse reactions between $CsPbBr_3$ and $CsPb_2Br_5$ and the corresponding changes of structure and morphologies. The thermally evaporated compact pristine layer was depicted in Figure S8, which showed small size grains and low crystallinity at room temperature and 200 °C. The yellow color of sample (Figure

S9) suggested the co-existence of $CsPbBr_3$ and derivative phases in the pristine film (Figure 3a, Figure S10a, b). As the annealing temperature increased, the color of as-prepared film gradually turned white (250 °C) and the grains grew quickly from 100 nm to 1 μm (Figure 3b) because of diffusion and reaction between precursor materials of CsBr and $PbBr_2$, which indicated the appearance of $CsPb_2Br_5$ in the as-prepared film. Subsequent increase of temperature (300 °C) led to further grain size growth of $CsPb_2Br_5$ with some grains reaching more than 5 μm (Figure 3b, c, Steps (1) and (2)). $CsPb_2Br_5$ is a PL-inactive semiconductor material with a wide bandgap of ~2.9 eV, indicating that it shows almost no photoluminescence under 365 nm irradiation as seen in Figure S8.[50, 51] However, the $CsPb_2Br_5$ phase is unstable at high temperature or humidity conditions and induces the self-decomposition (inverse reaction, $CsPb_2Br_5 \rightarrow CsPbBr_3 + PbBr_2 \uparrow$) as discussed before.[40] Therefore, when the annealing temperature increased further, starting from the grain boundaries, the large $CsPb_2Br_5$ grains decomposed to several small $CsPbBr_3$ crystallites forming the $CsPb_2Br_5$@$CsPbBr_3$ intermediate phase.[41, 51] The green color could be detected at the edge of the film under 365 nm irradiation in Figure S9 (~300 °C), which corroborates the formation of $CsPbBr_3$. In this case (Figure 3c, step (3)), $CsPb_2Br_5$ served as extra heterogeneous nucleation sites and also provided sufficient $CsPbBr_3$ that was originated from self-decomposition. $PbBr_2$ has a lower melting temperature (357 °C) than CsBr (630 °C).[41] Therefore, when the annealing temperature was close to this melting temperature (~350 °C), the excess $PbBr_2$ was melted/vaporized gradually, which would reduce the concentration of $PbBr_2$ and promote decomposition of $CsPb_2Br_5$ in a controlled way. In

parallel, because of the volatility of $PbBr_2$ at a high temperature of 916 °C, $PbBr_2$ at grain boundaries or edges began to evaporate slowly. Therefore, it would take a long time to complete this process. According to the Ostwald ripening theory, the small $CsPbBr_3$ particles generated during decomposition had a high surface energy and tend to dissolve and grew together to become a large particle in a closed system to reduce this energy (Figure 3c, step (3) and (4)).[42] The largest size of $CsPbBr_3$ was 10 μm (Figure 3b). It was noted that the appearance of phase transition from $CsPb_2Br_5$ to $CsPbBr_3$ with volatilization of $PbBr_2$, instead of the direct forward reaction from CsBr and $PbBr_2$, could slow down the formation of $CsPbBr_3$ crystals at a high temperature. As the treatment temperature rose to 400 °C, $CsPbBr_3$ with large grain sizes with high crystallinity and some aligned grain boundaries could be detected in Figure 3b. Correspondingly, the XRD data in Figure S10e revealed that the $CsPbBr_3$ crystal phase is the major phase in the film after treatment at 400 °C, although there still existed a few remnant peaks corresponding to the $CsPb_2Br_5$ phase or other intermediate states. In addition, it was noticed that the relative intensity of $CsPbBr_3$ (100)/ (200) peaks was much higher than that of $CsPbBr_3$ (110) peak in comparison with the $CsPbBr_3$ standard PDF card (PDF # 54-0752), which indicated that the $CsPbBr_3$ crystals were grown along the (100) direction. Enhanced photoluminescence with green color was observed under 365 nm irradiation (Figure S9), which could be explained by the formation of high quality of $CsPbBr_3$ crystals and consumption of the indirect bandgap material of $CsPb_2Br_5$, reducing the nonradiative recombination and improving the charge transport process.[52] As we continued to heat the sample to even higher temperatures, for example,

450 °C, the SEM image in Figure 3b presented a high crystallinity and aligned grains. The corresponding XRD patterns in Figure S10f displayed two main peaks at 15.20° and 30.66° indexed to the $CsPbBr_3$ (100) and (200) crystal planes, suggesting the high crystallization of the $CsPbBr_3$ phase with an orientation along (100) and disappearance of $CsPb_2Br_5$ (Figure 3c, step (5)). This preferred growth was possibly because the consumption of 2D $CsPb_2Br_5$ provided enough space for the crystal rearrangement from a 2D layer to a 3D cubic structure.[41] Besides, $CsPbBr_3$ has a higher decomposition/evaporation temperature (~580 °C) than $PbBr_2$.[53] The volatile $PbBr_2$ as a byproduct further facilitated the proposed phase transformation process and no external residues remained in the final products, which allowed us to achieve a high quality $CsPbBr_3$ crystals. Upon subsequent extended annealing time (from 20 min to 1h at 450 °C, Figure 3b), the $CsPbBr_3$ grains continuously grew and $PbBr_2$ desorbed preferentially from the edges of $CsPbBr_3$ grains leading to physical separation from the adjacent grains. After one hour annealing at 450 °C, a long $CsPbBr_3$ MW were obtained. Additionally, if the annealing time was prolonged to 1.5 h, some MWs break into several disconnect MWs with short length as seen in Figure S11. To realize MWs with long lengths, we also investigated the influence of the thickness of the precursor $CsPb_2Br_5$ film on the length of $CsPbBr_3$ MWs, because the formation of MWs depended on decomposition of $CsPb_2Br_5$. As we gradually increased the film thickness of $CsPb_2Br_5$ from 200 nm to 1000 nm, both the length and the diameter of the $CsPbBr_3$ MWs increased (Figure S12-S13). This could be explained as the thicker layer was beneficial for the growth of the compact perovskite film compared with the thin layer

growth, which resulted in the formation of perovskite grains with larger sizes during high temperature annealing.

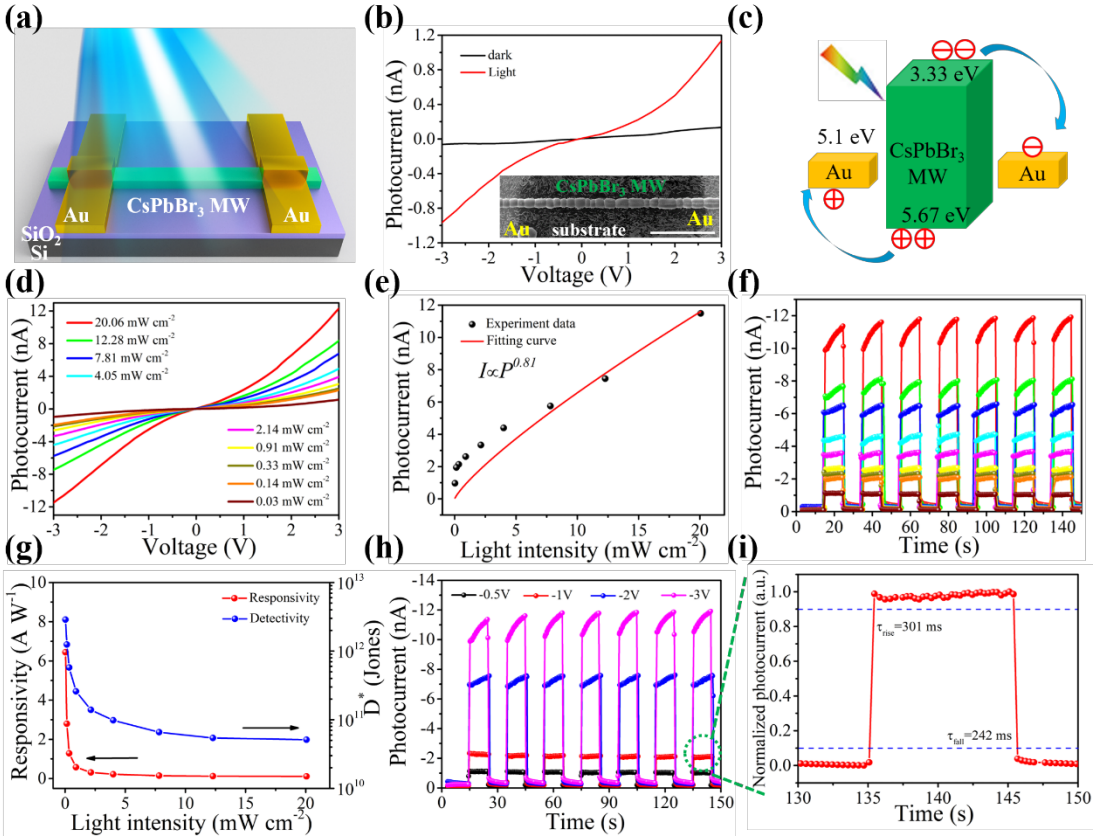

Figure 4. (a) Schematic illustration showing a $CsPbBr_3$ MW photodetector. (b) I-V curves of the $CsPbBr_3$ MW photodetector under dark and light (400 nm, 30 μW cm^{-2}) condition. SEM image of device is shown as the inset, and the scale bar is 40 μm. (c) Energy band diagram of device. (d) I-V curves and (f) I-t curves of the $CsPbBr_3$ MW photodetector under light with a wavelength of 400 nm and different intensities. (e) Photocurrent and g) responsivity/detectivity of the device as a function of irradiated intensities. (h) I-t curves of the $CsPbBr_3$ MW photodetector under different bias at 400 nm, 20.06 mW cm^{-2}. (i) Response time of the device during one-cycle.

A single $CsPbBr_3$ MW photodetector (PD) was fabricated as depicted in Figure 4a.

80 nm Au layer was deposited on the top surface of MW with a 100 μm spacing by a shadow mask to construct a device (Figure 4b, inset). The well distribution of grain size ranges from 3 μm to 11.5 μm (Figure S14) ensure light capture and carrier transport. In addition, as mentioned above, despite the MW shows us a polycrystalline structure, each grain is single crystal structure, which indicates lower trap defects in the grains. Figure S15 shows the photoresponsivity spectrum of a $CsPbBr_3$ MW under a fixed bias voltage of -5 V. As we can see, the device exhibits a high photoresponsivity in the region between 350 and 600 nm, which is consistent with the absorption spectrum. Figures 4b and S16 show the photocurrent-voltage (I-V) curves of the $CsPbBr_3$ MW PD under 400 nm light irradiation and dark conditions. A linear relationship suggested that an Ohmic-contact between MW and electrode was formed, which would accelerate the carrier transport under built-in electric field (Figure 4c). The photocurrent of the device increased by more than one order of magnitude under 400 nm (~30 μW cm^{-2}) irradiation compared to dark current. The corresponding responsivity (R) and detectivity (D^*) are extracted from the equation as follows:[54-56]

$$R = \frac{I_{light} - I_{dark}}{PA} \quad (1)$$

$$D^* = \frac{R\sqrt{AB}}{i_n} = R\sqrt{\frac{A}{2qI_{dark}}} \quad (2)$$

where I_{light} and I_{dark} are the photocurrent and dark current, respectively. P is the power intensity; q is the elementary charge; A is the active area; B is the electrical bandwidth of noise measurements; i_n is the noise current. Here, the MW is regarded as a rectangular-shaped structure and the corresponding active area is estimated as

follows:[26] A = a × b; a is the width of the nanowire (1 μm) and b is the length of the channel (100 μm). The dark current and photocurrent were -6.35×10^{-11} A and -9.66×10^{-10} A under a bias of −3 V, respectively. The lower dark current is ascribed to i) High crystallinity of each grain shows low defects; ii) The existence of grain boundaries (GBs) serving as energy barriers for carrier transport under a bias voltage in dark condition, which could effectively suppress the dark current of $CsPbBr_3$ MW PD.[57] On the other hand, under incident light irradiation, excessive photo-generated holes could quickly migrate to GBs due to the p-type of perovskite materials, which could effectively lower the energy barrier height and promote carrier transport under the internal electric field.[57] It is assumed that the dark current is dominated by the shot noise for estimating detectivity.[55] Therefore, the corresponding R and D^* are estimated to be 6.44 A W^{-1} and 2.88×10^{12} Jones (Jones = cm $Hz^{1/2}$ W^{-1}), respectively. To further evaluate the performance of the $CsPbBr_3$ MW PD, we conducted the photocurrent-voltage tests under different light intensities from 30 μW cm^{-2} to 20.06 mW cm^{-2} under 400 nm illumination (Figure 4d). The photocurrent rose sharply as the light intensity increased and the photocurrent of the device showed a strong dependence on the irradiation intensity with a best fitting of $I=P^{\theta}$, where I and P are the photocurrent and irradiation, respectively. θ is a proportionality constant related to recombination processes of photo-generated carriers. By fitting the curve in Figure 4e, we extracted θ = 0.81 for 400 nm irradiation that is close to the ideal value of 1, which suggested low recombination in the device and exhibited a good linearity for light detection.[58] In addition, the device also showed an excellent response characteristic measured by the

time-dependent photocurrent (I-t) at various intensities (from 0.03 mW cm^{-2} to 20.06 mW cm^{-2}) under a bias voltage of –3 V (Figure 4f). The photocurrent increased sharply when the light was turned on and also dropped fast when the light was turned off. Importantly, the $CsPbBr_3$ MW PD showed a stable and repeatable current under the light ON/OFF process upon the increase in power intensity. It was worth noting that the R and D^* values, as seen in Figure 4g, decreased significantly with the enhancement of irradiation power intensity. This reduction could be explained by the increased carrier recombination by deep traps or surface defects when the device was under strong light irradiation.[59] Besides the power intensity, the operational bias voltage also showed influence on the device. We compared the I-t curves of the device under –0.5 V, –1 V, –2 V and –3 V under 400 nm, ~20.06 mW cm^{-2} irradiation. The corresponding photocurrent improved monotonously from 1.02 nA to 11. 8 nA and showed a stable and repeatable states under light ON/OFF process (Figure 4h). Moreover, the response speed is another key parameter for PDs, which reflects the sensitivity to the incident light. As depicted in Figure 4i, the device showed a fast response time of 301/242 ms under 400 nm irradiation.

The stability of inorganic perovskite devices is affected by several factors including interface diffusion, phase transition to the non-perovskite structure, light irradiation and thermal/humidity conditions. To investigate the storage stability, we placed the device in air (RH ~ 45%) for over two months without any encapsulation. As depicted in Figure 5a, the device exhibited excellent durability against humidity and a long-term stable and repeatable performance under light ON/OFF cycles.

Furthermore, investigation of operational stability of devices under continuous light illumination is also important considering practical applications. Song and coworkers reported a $CsPbBr_3$ single crystal PD and found that the device are able to keep almost the same photocurrent as the initial value (loss of only 2.1%) over 360 min.[60] Here, we studied the operational stability of $CsPbBr_3$ MW PDs under 400 nm (20.06 mW cm^{-2}) illumination at bias voltage of −3 V. The photocurrent of the device remained ~70% of the initial performance after 3000 min (Figure 5b), which shows enhanced stability than the previous reports (Table 1). This performance improvement is originated from the larger grain size, high crystallinity and bigger thickness. Decomposition of perovskite materials usually starts at GBs after long term illumination, where water and oxygen easily penetrate into the perovskites resulting in continuous decomposition/degradation because of weaker chemical binding and ion migration at GBs in low crystallinity perovskites.[61, 62] Different from many GBs in the polycrystalline thin films, the less GBs in the MWs can effectively alleviate the moisture attacks. Besides, the extra top layer of the high-quality crystallites in the thicker grains (Height ~ 1.36 μm) of the MWs naturally protect the inner crystallites from degradation in comparison of thin height of single crystal NWs (Table 1).[61]

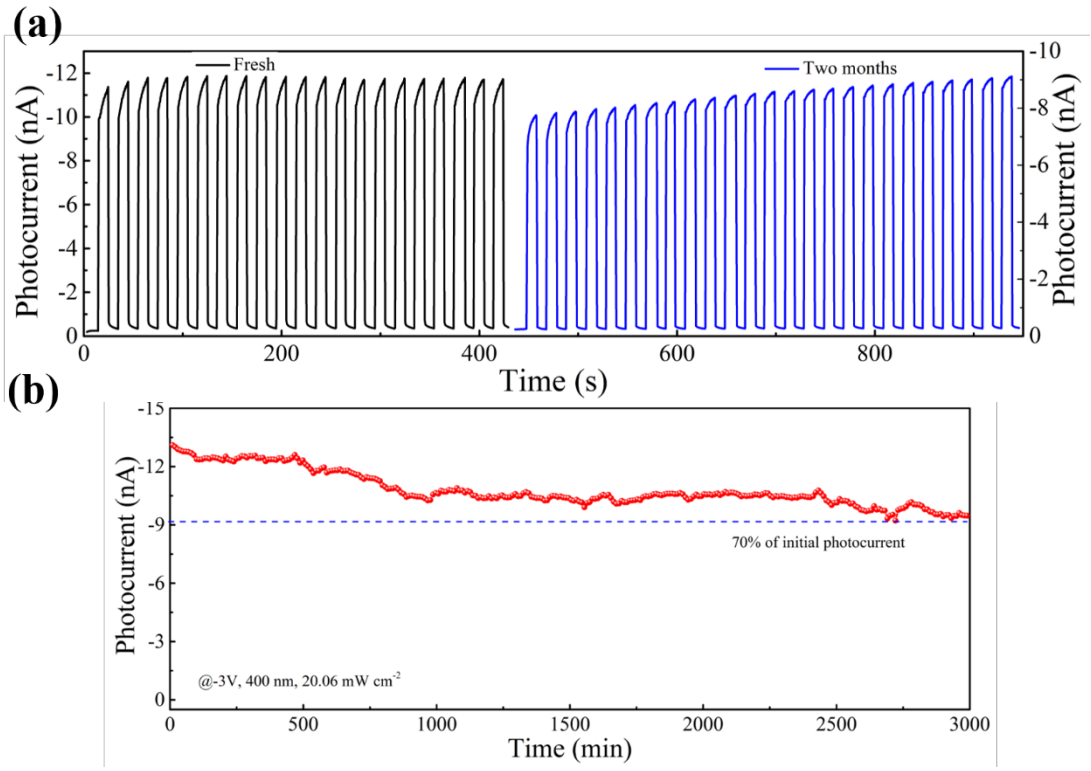

Figure 5. (a) I-t curve of the $CsPbBr_3$ MW photodetector taken shortly after fresh fabrication (black curve) and after storage in air (RH ~ 45%) (blue curve) for over two months (400 nm, ~20.06 mW cm^{-2}). (b) Operational stability of the $CsPbBr_3$ MW photodetector under a bias of −3 V and light illumination (400 nm, ~20.06 mW cm^{-2}).

3. CONCLUSION

In summary, we demonstrated an inverse growth method to achieve ultralong $CsPbBr_3$ MW (~510 μm) by controlling the decomposition of 2D $CsPb_2Br_5$ layer. This inverse growth mechanism allowed us to control the length of nanowire by regulating the thickness of $CsPb_2Br_5$ precursor layer. The high temperature procedure also ensured us to obtain a high crystalline $CsPbBr_3$ MW with large grain size. An outstanding performance of $CsPbBr_3$ MW photodetector was realized with an impressive responsivity of 6.44 A W^{-1} and detectivity of ~10^{12} Jones. Importantly, the device exhibited an excellent storage stability (RH~45%) for more than two months and

operational stability for over 3000 min. Overall, this inverse growth of $CsPbBr_3$ MW displayed to be a simple, yet controllable and versatile technique to make highly crystalline lead halide perovskite MWs and high performance photoelectronic devices.

METHODS

$CsPbBr_3$ nanowires and photodetectors. All chemicals were purchased from TCI (99%). The p-type silicon (100) substrates with a 300 nm thermal oxide layer (SiO_2) were purchased from Nova Electronic Materials. The substrates were cleaned by acetone, ethyl alcohol and deionized water, respectively. First, the 304 nm CsBr and 696 nm $PbBr_2$ films were sequentially deposited on the substrates by thermal evaporation with a rate of ~1 Å/s to achieve 1 μm $CsPb_2Br_5$ layer in the vacuum chamber with a vacuum degree of ~10^{-3} Pa. The density and Z factor of CsBr were set as 4.44 g cm^{-3} and 1.414, respectively. The corresponding parameters of $PbBr_2$ were 6.69 g cm^{-3} and 1.000, respectively. The thickness of films is well monitored by the quartz crystal microbalance. To synthesize the $CsPbBr_3$ nanowires, the as-prepared samples were annealed at 450 °C for 1 hour. Thermally evaporated 80 nm gold deposited on the MWs was used as electrodes. The devices were defined by a metal shadow mask with a width of 100 μm. The STEM samples were prepared by the same procedure on the silicon dioxide grids (TedPella, 40 nm membrane thickness) with a thickness of 30 nm precursor layer. The thickness of CsBr and $PbBr_2$ precursor layers were 9 nm and 21 nm, respectively.

Characterization. Surface morphologies were investigated by a field emission scanning electron microscopy (SEM, Helios NanoLab G3 UC) and a scanning transmission electron microscopy (STEM, JEM-ARM 200F). A silicon dioxide grid (purchased from TED PELLA, INC.) was employed in STEM. The crystal structure was determined by X-ray diffraction (XRD, Bruker AXS GmbH, Karlsruhe, Germany) equipped with Cu wavelength λ = 1.54 Å from 10 to 40° two theta degrees. AFM

measurements were performed in tapping mode with a frequency of ~ 71 KHz using an Asylum AFM (Asylum Co. MFP-3D-SA-DV-OQ). The scanning area of sample was 5×5 μm^2. All the electrical tests were conducted in the Lakeshore probe station (CRX-6.5K), the corresponding data were collected by a semiconductor parameter analyzer system (Keithley 4200-SCS). Monochromatic light was produced by a portable solar simulator combined with a 400 nm filter slice (THORLABS, FGK01S). The light intensities were calibrated by a power meter (THORLABS). All the procedures were performed in air (~45% relative humidity and 25 ^oC) without any encapsulation.

ASSOCIATED CONTENT

Supporting Information

The Supporting Information is available free of charge on the ACS Publications website at DOI: 10.1021/acsami. XXXX.

EDS mapping and line scan, SEM, XRD and AFM images of $CsPbBr_3$ MWs; Optical, XRD and SEM images of as-prepared $CsPb_2Br_5$ samples at different annealing temperatures; Grain size distribution of $CsPbBr_3$ MWs; Responsivity spectrum and I-V curve of $CsPbBr_3$ MWs photodetector.

AUTHOR INFORMATION

Corresponding Author
*E-mail: Yabing.Qi@OIST.jp

Notes

The authors declare no competing financial interest.

ACKNOWLEDGEMENTS

This work was supported by funding from the Energy Materials and Surface Sciences Unit of the Okinawa Institute of Science and Technology Graduate University, the OIST R&D Cluster Research Program, and the OIST Proof of Concept (POC) Program.

REFERENCES

(1) Tai, Q.; Tang, K.-C.; Yan, F. Recent Progress of Inorganic Perovskite Solar Cells. *Energy Environ. Sci.* **2019**, *12*, 2375-2405.

(2) Park, K.; Lee, J. W.; Han, J. D.; Jang, D. M.; Jeong, S.; Park, J.; Song, J. K. Light-Matter Interactions in Cesium Lead Halide Perovskite Nanowire Lasers. *J. Phys. Chem. Lett.* **2016**, *7*, 3703-3710.

(3) Du, P.; Li, J.; Wang, L.; Liu, J.; Li, S., Liu, N.; Li, Y.; Zhang, M.; Gao, L.; Ma, Y.; Tang, J. Vacuum-Deposited Blue Inorganic Perovskite Light-Emitting Diodes. *ACS Appl. Mater. Interfaces* **2019**, 11, 47083- 47090.

(4) Yang, L.; Tsai, W.-L.; Li, C.-S; Hsu, B.-W; Chen, C.-Y; Wu, C.-I; Lin, H.-W. High-Quality Conformal Homogeneous All-Vacuum Deposited $CsPbCl_3$ Thin Films and Their UV Photodiode Applications. *ACS Appl. Mater. Interfaces* **2019**, 11, 47054-47062.

(5) Zhao, L.; Gao, Y.; Su, M.; Shang, Q.; Liu, Z.; Li, Q.; Wei, Q.; Li, M.; Fu, L.; Zhong, Y.; Shi, J.; Chen, J.; Zhao, Y.; Qiu, X.; Liu, X.; Tang, N.; Xing, G.; Wang, X.; Shen, B.; Zhang, Q. Vapor-Phase Incommensurate Heteroepitaxy of Oriented Single-Crystal $CsPbBr_3$ on GaN: Toward Integrated Optoelectronic Applications. *ACS Nano* **2019**, *13*, 10085-10094.

(6) Chen, T.; Tong, G.; Xu, E.; Li, H.; Li, P.; Zhu, Z.; Tang, J.; Qi, Y. B.; Jiang, Y. Accelerating Hole Extraction by Inserting 2D Ti_3C_2-MXene Interlayer to All Inorganic Perovskite Solar Cells with Long-Term Stability. *J. Mater. Chem. A* **2019**, *7*, 20597-20603.

(7) Zhang, X.; Chen, S.; Wang, X.; Pan, A. Controlled Synthesis and Photonics Applications of Metal Halide Perovskite Nanowires. *Small Methods* **2019**, *3*,1800294.

(8) Gao, Y.; Zhao, L.; Shang, Q.; Zhong, Y.; Liu, Z.; Chen, J.; Zhang, Z.; Shi, J.; Du, W.; Zhang, Y.; Chen, S.; Gao, P.; Liu, X.; Wang, X.; Zhang, Q. Ultrathin $CsPbX_3$ Nanowire Arrays with Strong Emission Anisotropy. *Adv. Mater.* **2018**, *30*, 801805.

(9) Liu, J.; Song, K.; Shin, Y.; Liu, X.; Chen, J.; Yao, K. X.; Pan, J.; Yang, C.; Yin, J.; Xu, L.-J.; Yang, H.; El-Zohry, A. M.; Xin, B.; Mitra, S.; Hedhili, M. N.; Roqan, I. S.; Mohanmmed, O. F.; Han, Y.; Barkr, O. M. Light-Induced Self-Assembly of Cubic $CsPbBr_3$ Perovskite Nanocrystals into Nanowires. *Chem. Mater* **2019**, *31*, 6642-6649.

(10) Chen, G.; Feng, J.; Gao, H.; Zhao, Y.; Pi, Y.; Jiang, X.; Wu, Y.; Jiang, L. Stable α-$CsPbI_3$ Perovskite Nanowire Arrays with Preferential Crystallographic Orientation for Highly Sensitive Photodetectors. *Adv. Funct. Mater.* **2019**, *29*, 1808741.

(11) Oksenberg, E.; Sanders, E.; Popovitz-Biro, R.; Houben, L.; Joselevich E. Surface-Guided $CsPbBr_3$ Perovskite Nanowires on Flat and Faceted Sapphire with Size-Dependent Photoluminescence and Fast Photoconductive Response. *Nano Lett.* **2018**, *18*, 424-433.

(12) Eaton, S. W.; Lai, M.; Gibson, N. A.; Wong, A. B.; Dou, L.; Ma, J.; Wang, L.-W.; Leone, S. R.; Yang, P. Lasing in robust cesium lead halide perovskite nanowires. *Proc. Natl. Acad. Sci. USA* **2016**, *113*, 1993-1998.

(13) Yang, T.; Zheng, Y.; Du, Z.; Liu, W.; Yang, Z.; Gao, F.; Wang, L.; Chou, K.-C.; Hou, X.; Yang, W. Superior Photodetectors Based on All-Inorganic Perovskite $CsPbI_3$ Nanorods with Ultrafast Response and High Stability. *ACS Nano* **2018**, *12*, 1611-1617.

(14) Cao, F.; Tian, W.; Wang, M.; Cao, H.; Li, L. Semitransparent, Flexible, and Self-Powered Photodetectors Based on Ferroelectricity-Assisted Perovskite Nanowire Arrays. *Adv. Funct. Mater.* **2019**, *29*, 1901280.

(15) Waleed, A.; Tavakoli, M. M.; Gu, L.; Wang, Z.; Zhang, D.; Manikandan, A.; Zhang, Q.; Zhang, R.-J.; Chueh, Y.-L.; Fan, Z. Lead-Free Perovskite Nanowire Array Photodetectors with Drastically Improved Stability in Nanoengineering Templates. *Nano Lett.* **2017**, *17*, 523-530.

(16) Zhou, Q.; Park, J. G.; Nie, R.; Thokchom, A. K.; Ha, D.; Pan, J.; Pan, J.; Seok, S. Il.; Kim, T. Nanochannel-Assisted Perovskite Nanowires: From Growth Mechanisms to Photodetector Applications. *ACS Nano* **2018**, *12*, 8406-8414.

(17) Shoaib, M.; Zhang, X.; Wang, X.; Zhou, H.; Xu, T.; Wang, X.; Hu, X.; Liu, H.; Fan, X.; Zheng, W.; Yang, T.; Yang, S.; Zhang, Q.; Zhu, X.; Sun, L.; Pan, A. Directional Growth of Ultralong $CsPbBr_3$ Perovskite Nanowires for High-Performance Photodetectors. *J. Am. Chem. Soc.* **2017**, *139*, 15592-15595.

(18) Deng, W.; Zhang, X.; Huang, L.; Xu, X.; Wang, L.; Wang, J.; Shang, Q.; Lee, S.-

T.; Jie, J. Aligned Single-Crystalline Perovskite Microwire Arrays for High-Performance Flexible Image Sensors with Long-Term Stability. *Adv. Mater.* **2016**, *28*, 2201-2208.

(19) Feng, J.; Yan, X.; Liu, Y.; Gao, H.; Wu, Y.; Su, B.; Jiang, L. Crystallographically Aligned Perovskite Structures for High-Performance Polarization-Sensitive Photodetectors. *Adv. Mater.* **2017**, *29*, 1605993.

(20) Zhang, D.; Yang, Y.; Bekenstein, Y.; Yu, Y.; Gibson, N. A.; Wong, A. B.; Eaton, S. W.; Kornienko, N.; Kong, Q.; Lai, M.; Alivisatos, A. P.; Leone, S. R.; Yang, P. Synthesis of Composition Tunable and Highly Luminescent Cesium Lead Halide Nanowires through Anion-Exchange Reactions. *J. Am. Chem. Soc.* **2016**, *138*, 7236-7239.

(21) Tong, G.; Geng, X.; Yu, Y.; Yu, L.; Xu, J.; Jiang, Y.; Sheng, Y.; Chen, K. Rapid, Stable and Self-Powered Perovskite Detectors via a Fast Chemical Vapor Deposition Process. *RSC Adv.* **2017**, *7*, 18224-18230.

(22) Zhou, H.; Yuan, S.; Wang, X.; Xu, T.; Wang, X.; Li, H.; Zheng, W.; Fan, P.; Li, Y.; Sun, L.; Pan, A. Vapor Growth and Tunable Lasing of Band Gap Engineered Cesium Lead Halide Perovskite Micro/Nanorods with Triangular Cross Section. *ACS Nano* **2017**, *11*, 1189-1195.

(23) Waleed, A.; Tavakoli, M. M.; Gu, L.; Hussain, S.; Zhang, D.; Poddar, S.; Wang, Z.; Zhang, R.; Fan, Z. All Inorganic Cesium Lead Iodide Perovskite Nanowires with Stabilized Cubic Phase at Room Temperature and Nanowire Array-Based Photodetectors. *Nano Lett.* **2017**,*17* ,4951-4957.

(24) Wang, Y.; Yasar, M.; Luo, Z.; Zhou, S.; Yu, Y.; Li, H.; Yang, R.; Wang, X.; Pan, A.; Gan, L.; Zhai, T. Temperature Difference Triggering Controlled Growth of All-Inorganic Perovskite Nanowire Arrays in Air. *Small* **2018**, *14*, 1803010.

(25) Creighton, J. R.; Ho, P. Introduction to Chemical Vapor Deposition (CVD). *ASM International: Materials Park*, OH, **2001**, 1-22.

(26) Meng, Y.; Lan, C.; Li, F.; Yip, S.; Wei, R.; Kang, X.; Bu, X.; Dong, R.; Zhang, H.; Ho, J. C. Direct Vapor-Liquid-Solid Synthesis of All-Inorganic Perovskite Nanowires for High-Performance Electronics and Optoelectronics. *ACS Nano* **2019**, *13*, 6060-6070.

(27) Pauzauskie, P. J.; Yang, P. Nanowire photonics. *Materials Today* **2006**, *9*, 36-45.

(28) Chen, J.; Fu, Y.; Samad, L.; Dang, L.; Zhao, Y.; Shen, S.; Guo, L.; Jin, S. Vapor-Phase Epitaxial Growth of Aligned Nanowire Networks of Cesium Lead Halide Perovskites ($CsPbX_3$, X = Cl, Br, I). *Nano Lett.* **2017**, *17*, 460-466.

(29) Chen, J.; Luo, Z.; Fu, Y.; Wang, X.; Czech, K.; Shen, S.; Guo, L.; Wright, J. C.; Pan, A.; Jin, S. Tin (IV)-Tolerant Vapor-Phase Growth and Photophysical Properties of Aligned Cesium Tin Halide Perovskite ($CsSnX_3$; X=Br, I) Nanowires. *ACS Energy Lett.* **2019**, *4*, 1045-1052.

(30) Meyers, J. K.; Kim, S.; Hill, D. J.; Cating, E. E. M.; Williams, L. J.; Kumbhar, A.; McBride, J. R.; Papanikolas, J. M.; Cahoon, J. F. Self-Catalyzed Vapor-Liquid-Solid Growth of Lead Halide Nanowires and Conversion to Hybrid Perovskites. *Nano Lett.* **2017**,*17*, 7561-7568.

(31) Wang, Y.; Sun, X.; Shivanna, R.; Yang, Y.; Chen, Z.; Guo, Y.; Wang, G.-C.; Wertz,

E.; Deschler, F.; Cai, Z.; Zhou, H.; Lu, T.-M.; Shi, J. Photon Transport in One-Dimensional Incommensurately Epitaxial $CsPbX_3$ Arrays. *Nano Lett.* **2016**, *16*, 7974-7981.

(32) Yang, Z.; Lu, J.; ZhuGe, M.; Cheng, Y.; Hu, J.; Li, F.; Qiao, S.; Zhang, Y.; Hu, G.; Yang, Q.; Peng, D.; Liu, K.; Pan, C. Controllable Growth of Aligned Monocrystalline $CsPbBr_3$ Microwire Arrays for Piezoelectric-Induced Dynamic Modulation of Single-Mode Lasing. *Adv. Mater.* **2019**, *31*, 1900647.

(33) Zhou, Y.; Luo, J.; Zhao, Y.; Ge, C.; Wang, C.; Gao, L.; Zhang, C.; Hu, M.; Niu, G.; Tang, J. Flexible Linearly Polarized Photodetectors Based on All-Inorganic Perovskite $CsPbI_3$ Nanowires. *Adv. Optical Mater.* **2018**, *6*, 1800679.

(34) Tong, G.; Chen, T.; Li, H.; Song, W.; Chang, Y.; Liu, J.; Yu, L.; Xu, J.; Qi, Y.B.; Jiang, Y. High Efficient Hole Extraction and Stable All-Bromide Inorganic Perovskite Solar Cells via Derivative-Phase Gradient Bandgap Architecture. *Sol. RRL* **2019**, *5*, 1900030.

(35) Chen, J.; Morrow, D. J.; Fu, Y.; Zheng, W.; Zhao, Y.; Dang, L.; Stolt, M. J.; Kohler, D. D.; Wang, X.; Czech, K. J.; Hautzinger, M. P.; Shen, S.; Guo, L.; Pan, A.; Wright, J. C.; Jin, S. Single-Crystal Thin Films of Cesium Lead Bromide Perovskite Epitaxially Grown on Metal Oxide Perovskite ($SrTiO_3$). *J. Am. Chem. Soc.* **2017**, *139*, 13525-13532.

(36) Kuo, T.-J.; Lin, C.-N.; Kuo, C.-L.; Huang, M. H. Growth of Ultralong ZnO Nanowires on Silicon Substrates by Vapor Transport and Their Use as Recyclable Photocatalysts. *Chem. Mater* **2007**, *19*, 5143-5147.

(37) Tong, G.; Li, H.; Zhu, Z.; Zhang, Y.; Yu, L.; Xu, J.; Jiang, Y. Enhancing Hybrid Perovskite Detectability in the Deep Ultraviolet Region with Down-Conversion Dual-Phase ($CsPbBr_3$-Cs_4PbBr_6) Films. *J. Phys. Chem. Lett.* **2018**, *9*, 1592-1599.

(38) Tong, G.; Li, H.; Li, G.; Zhang, T.; Li, C.; Yu, L.; Xu, J.; Jiang, Y.; Shi, Y.; Chen, K. Mixed Cation Perovskite Solar Cells by Stack-Sequence Chemical Vapor Deposition with Self-Passivation and Gradient Absorption Layer. *Nano Energy* **2018**, *48*, 536-542.

(39) Tong, G.; Li, H.; Li, D.; Zhu, Z.; Xu, E.; Li, G.; Yu, L.; Xu, J.; Jiang, Y. Dual-Phase $CsPbBr_3$-$CsPb_2Br_5$ Perovskite Thin Films via Vapor Deposition for High-Performance Rigid and Flexible Photodetectors. *Small* **2018**, *14*, 1702523.

(40) Palazon, F.; Dogan, S.; Marras, S.; Locardi, F.; Nelli, I.; Rastogi, P.; Ferretti, M.; Prato, M.; Krahne, R.; Manna, L. From $CsPbBr_3$ Nano-Inks to Sintered $CsPbBr_3$-$CsPb_2Br_5$ Films via Thermal Annealing: Implications on Optoelectronic Properties. *J. Phys. Chem. C* **2017**, *121*, 11956-11961.

(41) Tong, G.; Chen, T.; Li, H.; Qiu, L.; Liu, Z.; Dang, Y.; Song, W.; Ono, L. K.; Jiang, Y.; Qi, Y. B. Phase Transition Induced Recrystallization and Low Surface Potential Barrier Leading to 10.91%-Efficient $CsPbBr_3$ Perovskite Solar Cells. *Nano Energy* **2019**, *65*, 104015.

(42) Yang, M.; Zhang, T.; Schulz, P.; Li, Z.; Li, G.; Kim, D. H.; Guo, N.; Berry, J. J.; Zhu, K.; Zhao, Y. Facile Fabrication of Large-Grain $CH_3NH_3PbI_{3-x}Br_x$ Films for High-Efficiency Solar Cells via CH_3NH_3Br-Selective Ostwald Ripening. *Nat. Commun.* **2016**, *7*, 12305.

(43) Baldan, A. Review Progress in Ostwald Ripening Theories and Their Applications to Nickel-Base Superalloys Part I: Ostwald Ripening Theories. *J. Mater. Sci.* **2002**, *37*, 2171-2202.

(44) Lai, M.; Kong, Q.; Bischak, C. G.; Yu, Y.; Dou, L.; Eaton, S. W.; Ginsberg, N. S.; Yang, P. Structural, Optical, and Electrical Properties of Phase-Controlled Cesium Lead Iodide Nanowires. *Nano Research* **2017**, *10*, 1107-1114.

(45) Tang, X.; Zu, Z.; Shao, H.; Hu, W.; Zhou, M.; Deng, M.; Chen, W.; Zang, Z.; Zhu, T.; Xue, J. All-Inorganic Perovskite $CsPb(Br/I)_3$ Nanorods for Optoelectronic Application. *Nanoscale* **2016**, *8*, 15158-15161.

(46) Pradhan, B.; Kumar, G. S.; Sain, S.; Dalui, A.; Ghorai, U. K.; Pradhan, S. K.; Acharya, S. Size Tunable Cesium Antimony Chloride Perovskite Nanowires and Nanorods. *Chem. Mater* **2018**, *30*, 2135-2142.

(47) Song, J.; Xu, L.; Li, J.; Xue, J.; Dong, Y.; Li, X.; Zeng, H. Monolayer and Few-Layer All-Inorganic Perovskites as a New Family of Two-Dimensional Semiconductors for Printable Optoelectronic Devices. *Adv. Mater.* **2016**, *28*, 4861-4869.

(48) Zhang, Z.; Li, C.; Lu, Y.; Tong, X.; Liang, F.; Zhao, X.; Wu, D.; Xie, C.; Luo, L. Sensitive Deep Ultraviolet Photodetector and Image Sensor Composed of Inorganic Lead-Free $Cs_3Cu_2I_5$ Perovskite with Wide Bandgap. *J. Phys. Chem. Lett.* **2019**, *10*, 5343-5350.

(49) Li, H.; Tong, G.; Chen, T.; Zhu, H.; Li, G.; Chang, Y.; Wang, L.; Jiang, Y. Interface Engineering using a Perovskite Derivative Phase for Efficient and Stable $CsPbBr_3$

Solar Cells. *J. Mater. Chem. A* **2018**, *6*, 14255-14261.

(50) Li, G.; Wang, H.; Zhu, Z.; Chang, Y.; Zhang, T.; Song, Z.; Jiang, Y. Shape and Phase Evolution from $CsPbBr_3$ Perovskite Nanocubes to Tetragonal $CsPb_2Br_5$ Nanosheets with an Indirect Bandgap. *Chem. Commun.* **2016**, *52*, 11296-11299.

(51) Wang, C.; Wang, Y.; Su, X.; Hadjiev, V. G.; Dai, S.; Qin, Z.; Benavides, H. A. C.; Ni, Y.; Li, Q.; Jian, J.; Alam, Md. K.; Wang, H.; Hernandez, F. C. R.; Yao, Y.; Chen, S.; Yu, Q.; Feng, G.; Wang, Z.; Bao, J. Extrinsic Green Photoluminescence from the Edges of 2D Cesium Lead Halides. *Adv. Mater.* **2019**, *31*, 1902492.

(52) Wang. Y.; Li. W.; Zhang. T.; Li. D.; Kan. M.; Wang. X.; Liu. X.; Wang. T.; Zhao. Y.; Highly Efficient (110) Orientated FA-MA Mixed Cation Perovskite Solar Cells via Functionalized Carbon Nanotube and Methylammonium Chloride Additive. *Small Methods* **2019**, 1900511.

(53) Kulbak, M.; Gupta, S.; Kedem, N.; Levine, I.; Bendikov, T.; Hodes, G.; Cahen, D. Cesium Enhances Long-Term Stability of Lead Bromide Perovskite-Based Solar Cells. *J. Phys. Chem. Lett.* **2016**, *7*, 167-172.

(54) Wu, D.; Guo, J.; Du, J.; Xia, C.; Zeng, L.; Tian, Y.; Shi, Z.; Tian, Y.; Li, X. J.; Tsang, Y. H.; Jie, J. Highly Polarization-Sensitive, Broadband, Self-Powered Photodetector Based on Graphene/$PdSe_2$/Germanium Heterojunction. *ACS Nano* **2019**, *13*, 9907-9917.

(55) Wang, L.; Jie, J.; Shao, Z.; Zhang, Q.; Zhang, X.; Wang, Y.; Sun, Z.; Lee, S.-T. MoS_2/Si Heterojunction with Vertically Standing Layered Structure for Ultrafast, High-Detectivity, Self-Driven Visible-Near Infrared Photodetectors. *Adv. Funct.*

Mater. **2015**, *25*, 2910-2919.

(56) Miao, J.; Zhang, F. Recent Progress on Photomultiplication Type Organic Photodetectors. *Laser Photonics Rev.* **2019**, *13*, 1800204.

(57) Liu, X.; Gu, L.; Zhang, Q.; Wu, J.; Long, Y.; Fan, Z. All-Printable Band-Edge Modulated ZnO Nanowire Photodetectors with Ultra-High Detectivity. *Nat. Commun.* **2014**, *5* 4007.

(58) Li, X.; Zhu, M.; Du, M.; Lv, Z.; Zhang, L.; Li, Y.; Yang, Y.; Yang, T.; Li, X.; Wang, K.; Zhu, H.; Fang, Y. High Detectivity Graphene-Silicon Heterojunction Photodetector. *Small* **2016**, *12*, 595-601.

(59) Zeng, L.-H.; Chen, Q.-M.; Zhang, Z.-X.; Wu, D.; Yuan, H.; Li, Y.-Y.; Qarony, W.; Lau, S. P.; Luo, L.-B.; Tsang, Y. H. Multilayered $PdSe_2$/Perovskite Schottky Junction for Fast, Self-Powered, Polarization-Sensitive, Broadband Photodetectors, and Image Sensor Application. *Adv. Sci.* **2019**, 1901134.

(60) Song, J.; Cui, Q.; Li, J.; Xu, J.; Wang, Y.; Xu, L.; Xue, J.; Dong, Y.; Tian, T.; Sun, H.; Zeng, H. Ultralarge All-Inorganic Perovskite Bulk Single Crystal for High-Performance Visible-Infrared Dual-Modal Photodetectors. *Adv. Optical Mater.* **2017**, *5*, 1700157.

(61) Liu, Z.; Qiu, L.; Juarez-Perez, M, J.; Hawash, Z.; Kim, T.; Jiang, Y.; Wu, Z.; Raga, S. R.; Ono, L. K.; Liu, S. F.; Qi, Y. B. Gas-Solid Reaction Based over One-Micrometer Thick Stable Perovskite Films for Efficient Solar Cells and Modules. *Nat. Commun*. **2018**, *9*, 3880.

(62) Chen, Z.; Dong, Q.; Liu, Y.; Bao, C.; Fang, Y.; Lin, Y.; Tang, S.; Wang, Q.; Xiao,

X.; Bai, Y.; Deng, Y.; Huang, J. Thin Single Crystal Perovskite Solar Cells to Harvest Below-Bandgap Light Absorption. *Nat. Commun*. **2017**, *8*, 1890.

TOC graph